

# Low load operating protocol investigation of a 620MWe power boiler using an indirectly coupled process model

B.T. Rawlins, R. Laubscher\*, P. Rousseau

*Department of Mechanical Engineering, Applied Thermal-Fluid Process Modeling Research Unit, University of Cape Town, Library Rd, Rondebosch, Cape Town, 7701, South Africa*

---

## Abstract

Low load operation of utility boiler ghfbksbv  
sfjvnsfjlv  
kfnmvknsfklvns  
lk;sfvnsfnvsd  
sk,vnsfk;nvk;sdv  
ksdnv;sdv  
sknvk

*Keywords:* CFD, Eulerian-Eulerian, Boiler, Low-load operation

---

## Nomenclature

### Symbols

$\dot{Q}_{conv}$	Convective heat transfer rate	$W$
$\dot{Q}_{rad}$	Radiative heat transfer rate	$W$
$\dot{Q}_w$	Wall heat transfer rate	$W$
$A$	Area	$m^2$
$A_p$	Particle surface area	$m^2$
$A_c$	Carbon pre-exponential factor	$s^{-1}$

---

\*Corresponding author

Email address: ryno.laubscher@uct.ac.za (R. Laubscher)

$A_{pn}$	Projected particle surface area	$m^2$
$A_{vol}$	Volatile pre-exponential factor	$s^{-1}$
$d_p$	Particle diameter	$m$
$E$	Fluid total energy	$J/kg$
$E_p$	Particle emission power	$W/m^3$
$E_{a,c}$	Carbon activation energy	$J/kmol$
$E_{a,vol}$	Volatile activation energy	$J/kmol$
$f_{heat}$	Near surface char oxidation fraction	—
$f_p$	Forward scattering factor	—
$G$	Incident radiation	$W/m^2$
$g$	Gravitational constant	$m/s^2$
$h_M$	Mixture enthalpy	$J/kg$
$h_{fg}$	Enthalpy of evaporation	$J/kg$
$h_{rxn}$	Enthalpy of reaction	$J/kg$
$J_k$	Species diffusion flux	$m^2/s$
$m_{0,vol}$	Original mass of volatiles	$kg$
$m_{char}$	Mass of carbon	$kg$
$m_{evap}$	Mass of moisture	$kg$
$m_{vol}$	Mass of volatiles	$kg$
$N_p$	Number of particles	—
$P$	Perimeter	$m$
$p$	Pressure	$Pa$
$p_{O_2}$	Partial pressure of $O_2$	$Pa$
$R$	Universal gas constant	$J/molK$
$R_c$	Carbon reaction rate	$s^{-1}$

$R_{diff}$	Diffusion reaction rate	$s^{-1}$
$R_{vol}$	Volatile reaction rate	$s^{-1}$
$t$	Time	$s$
$T_g$	Gas temperature	$K$
$T_p$	Particle temperature	$K$
$u$	Velocity	$m/s$
$V$	Volume	$m^3$
$x$	Quality	—
$Y_k$	Species mass fraction	$kg/kg$

#### **Greek symbols**

$\alpha_g$	Gas absorption coefficient	$m^{-1}$
$\alpha_H$	Mixture void fraction	—
$\alpha_p$	Particle absorption coefficient	$m^{-1}$
$\epsilon$	Emissivity	—
$\phi$	Scalar variable	—
$\rho$	Gas density	$kg/m^3$
$\rho_g$	Gas density	$kg/m^3$
$\rho_l$	Liquid density	$kg/m^3$
$\rho_M$	Mixture density	$kg/m^3$
$\rho_p$	Particle density	$kg/m^3$
$\rho_{eff}$	Effective density	$kg/m^3$
$\sigma_p$	Particle scattering coefficient	$m^{-1}$
$\sigma_{SB}$	Stefan-Boltzmann constant	$W/m^2K^4$

#### **Abbreviations**

<i>AR</i>	As-received
<i>ATT</i>	Attemperator
<i>CFD</i>	Computational fluid dynamics
<i>CFPP</i>	Coal fired power plant
<i>DAF</i>	Dry ash free
<i>EC</i>	Economiser
<i>EE</i>	Eulerian-Eulerian
<i>HHV</i>	Higher heating value
<i>MCR</i>	Maximum continuous rating
<i>PA</i>	Primary air
<i>RH</i>	Reheater
<i>RTE</i>	Radiative transport equation
<i>SA</i>	Secondary air
<i>SA – AH</i>	Secondary air - air heater
<i>SH</i>	Superheater
<i>WSGGM</i>	Weighted sum of gray gas model

## 1. Introduction

The use of coal fired power plants (CFPP) to provide electricity generation is intended to be phased out in order to mitigate the ingress of climate change. However, the switch to more sustainable generation sources pose great challenges  
5 for developing countries due to the long transition times and costs involved [1]. Due to the abundance of coal resource present in South Africa CFPPs are the dominant power generation source, with approximately 80 % of the energy needs being met using CFPPs [2]. The promising integration of renewable energy and the decommissioning of old CFPPs in South Africa, will push CFPP from a

10 primarily base load operation to a mid-merit/flexible operating protocol. This will inherently mean CFPPs will need to operate at low-loads for continuous time periods.

Mathematical models that can accurately capture the behaviour of the boilers thermal-hydraulic response at varying loads can be used to determine the safe and efficient operating limits [3]. Since, the long term deviation from design  
15 conditions can lead to operational incapacibilities affecting combustion stability [4], an increase in harmful emissions [5] and the localised overheating of heat exchangers due to insufficient cooling being provided by the internal working fluid [6].

20 The full scale testing or experimentation of CFPPs is deemed to expensive to pursue, thus the use of computational fluid dynamics (CFD) allows for the modelling of a full-scale CFPPs, at steady-state, to be investigated at various loads circumnavigating the use of time-consuming and costly field tests. CFD simulations have been successfully used to model a variety of CFPP boiler types  
25 ([7], [8]) and cover various aspects such as pollution control ([9],[10]), gas-solid flow effects ([11]) and boiler retrofitting ([8], [12]).

Recent CFD studies investigating low-load operation of CFPP boilers have focused on the combustion stability, harmful emissions and the gas flow-solid flow interactions [13]. The works of Belosevic et al [14] found that the low-load  
30 operation of boiler considerably affect the flow and temperature fields, the flame geometry, chemical reactions and concentrations of combustion products.

Hernik et al [4] investigated the effects of using different mill system configurations at a minimum boiler load of 40 %. The most favourable mill system configuration was selected based on the case that exhibited suitable combustion  
35 stability and emission of harmful substances. Similarly, Chang et al [5] investigated the various firing arrangements of a 630 *MWe* tangentially fired boiler. A burner angle of -15 ° was found to be the optimal arrangement resulting in the best compromise in combustion stability and lower emissions. However, to the best the authors' knowledge, no integration of 1-D thermal-hydraulic model  
40 has been used to investigate the steam side operational performance of a CFPP

boiler at low-load.

The use of a 1-D thermal-hydraulic modelling approach have been used by researchers to investigate the water and gas side heat transfer interactions. These studies are usually used to investigate a transient event, such as a sudden disturbance, start-up or boiler load ramping [15]. Due to the non-uniformities found in CFPP furnaces which are composed of complex combustion dynamics, gas-solid interactions and radiation heat transfer phenomena, 1-D thermal-hydraulic models can not resolve the fireside with sufficient accuracy, but can adequately resolve the waterside energy and momentum transport in a computationally inexpensive manner.

The use of coupled simulations has proven to solve the deficiencies of a full 1-D thermal-hydraulic model by coupling the fireside CFD to a 1-D water network. Recently Laubscher and Rousseau [16] conducted a comprehensive numerical study on the impact of particle radiation properties for high ash coals using ANSYS Fluent v19.2<sup>®</sup> and Flownex SE<sup>®</sup>. Yu et al [17] used a coupled simulation methodology to estimate the superheater (SH) metal temperatures of a 660 *MWe* tangentially-fired coal boiler.

The current work proposes the use of CFD modelling methodology to investigate the low-load operational combustion conditions and optimal burner firing arrangement of 620 *MWe* two-pass sub-critical boiler. Furthermore a process model of boilers entire system, including the furnace up till the secondary air-heater, was modelled, which was indirectly coupled to the CFD model, to investigate the necessary process controls needed to ensure; an adequate boiler utilization efficiency, sufficient attemperation/cooling of the radiant SH's and an exit main steam temperature supply of 535 °C.

The model was simulated for a boiler load of 32 % with 6 various firing combinations. To establish the accuracy of the CFD modelling approach a validation study was conducted for 100 %, 80 % and 60 % maximum continuous rating (MCR) loads and compared to actual plant measurements to quantify the model accuracy, this is highlighted in section 4.1 prior to the results of the low-load study.

## 2. Mathematical model

In this section the modelling techniques used by the study are elaborated. A description of the CFD modelling configuration is discussed focusing on the fluid flow, turbulence and combustion modelling as well as the particle transport field resolution. Following this is a description of the heat transfer modelling techniques and the ends with a description of the process modelling configuration.

### 2.1. Computational fluid dynamics modelling

#### 2.1.1. Fluid flow, turbulence and combustion modelling

The flue gas was modelled using a Eulerian framework. The species transport modelling approach was used to approximate the mixture of chemical species in the gas phase. This approach solves a species continuity equation for each constituent present in the mixture. To reduce the computational burden it was assumed that the various processes were in steady-state. The governing equations for the gas phase are written in their respective Reynolds averaged forms as follows;

Mass conservation:

$$\frac{\partial}{\partial x_i}(\rho \bar{u}_i) = S_m. \quad (1)$$

Momentum conservation:

$$\frac{\partial}{\partial x_i}(\rho_{eff} u_i u_j) + \frac{\partial \bar{p}}{\partial x_j} = \frac{\partial}{\partial x_i} \left[ \mu \left\{ \frac{\partial u_j}{\partial x_i} + \frac{\partial u_i}{\partial x_j} - \frac{2}{3} \delta_{ij} \frac{\partial u_i}{\partial x_i} \right\} \right] + \frac{\partial}{\partial x_i}(-\rho \overline{u'_i u'_j}) + S_m \quad (2)$$

Energy conservation:

$$\frac{\partial}{\partial x_i}(u_i[\rho E + p]) = \frac{\partial}{\partial x_j} \left[ \lambda \frac{\partial T_g}{\partial x_j} \right] + S_h \quad (3)$$

Species transport:

$$\frac{\partial}{\partial x_i}(\rho u_j Y_k) = -\frac{\partial}{\partial x_j}(\vec{J}_k) + \sum_r R_{j,r} + S_k \quad (4)$$

$$k = 1, 2, 3 \dots N$$

To correctly account for the particle inertial effects on the gas phase convection, the model makes use of an effective density is defined present as follows;

$$\rho_{eff} = \frac{\rho \rho_p (\phi_{mp} + 1)}{\rho \phi_{mp} + \rho_p} \quad (5)$$

In the present study the realizable k- $\epsilon$  turbulence model was utilized to address the turbulence closure problem. This model has been successfully used by researchers ([14],[7] and [6]), in modelling the effects of coal-fired swirl burners. The model generally generates higher accuracy results, when compared to the  
85 standard k- $\epsilon$  model, for problems incorporating swirling and separating flows.

The process of coal combustion comprises four steps. Namely, inert heating and evaporation of moisture, devolatilization, char oxidation and gas phase reactions. Equations (6) and (7) show the single rate kinetic model utilized in this study, to model the devolatilization process.

$$\frac{dm_{vol}}{dt} = R_{vol}(m_{0,vol} - m_{vol}) \quad (6)$$

$$R_{vol} = A_{vol} \exp\left(\frac{E_{a,vol}}{RT_p}\right) \quad (7)$$

$$A_{vol} = 2 \times 10^5 [s^{-1}] \quad E_{a,vol} = 6.7 \times 10^7 [J/kmol]$$

A devolatilization temperature of 553 [K] [18] along with the kinetic parameters (equation 7) of Sheng et al [19] were utilized. The char oxidation process is modelled using the diffusion-kinetics limited model developed by Baum and Street [20], which is given in equation (8). The product species of the char oxidation reaction was set to  $CO$  as shown in equation (9).

$$\frac{dm_{char}}{dt} = -A_p p_{O_2} \frac{R_{diff} R_c}{R_{diff} + R_c} \quad (8)$$





The diffusion and kinetic rates of equation (8) are defined in equations (10) and (11) with the kinetic parameters again taken from the works of Sheng et al [19].

$$R_{diff} = \frac{5 \times 10^{-12}}{d_p} \left( \frac{T_g + T_p}{2} \right)^{0.75} \quad (10)$$

$$R_c = A_c \exp \left( \frac{E_{a,c}}{RT_p} \right) \quad (11)$$

$$A_c = 0.0053 [kg/m^2 s Pa] \quad E_{a,c} = 8.37 \times 10^7 [J/kmol]$$

The turbulence-chemistry interactions of the gas phase reactions were approximated using the eddy-dissipation-finite rate model used in ANSYS Fluent v19.5<sup>®</sup> which calculates three rates, namely chemical reaction rate, turbulent production eddies dissipation rate and reaction eddies dissipation rate, and uses  
90 the minimum of the three for the source terms calculations. A description of the CFD gas phase reactions of the boiler under consideration, using the same coal, was previously published in the works of Laubscher and Rousseau [3].

### 2.1.2. Particle modelling

The particles are modelled using a Eulerian reference frame, similar to the  
95 studies of Knaus et al [21] and Benim et al [22], who both successfully used a multi-phase Eulerian-Eulerian (EE) model to capture the characteristics of coal combustion and furnace heat transfer with adequate accuracy. The pseudo particles transported into the domain are modelled using the general scalar field transport equation [23]. The pseudo-particles scalar fields are used to define  
100 the fuel characteristics based on the proximate analysis composition, namely consisting of moisture, volatile matter, fixed carbon and ash. Each of the scalar field equations are given in Table 1.

The energy transport of the pseudo particle, is transported by defining the particle enthalpy using the following equation:

$$\frac{\partial}{\partial x_i} (\rho u_i \phi_{hp}) = \left( f_{heat} \frac{dm_c}{dt} h_{rxn} + \dot{Q}_{rad} + \dot{Q}_{conv} - \frac{dm_{evap}}{dt} h_{fg} \right) \frac{1}{V} \quad (12)$$

The equation accounts for all the processes associated with energy transport to the particle, namely convection  $(\dot{Q}_{conv})$ , radiation  $(\dot{Q}_{rad})$ , latent heat

Table 1: Scalar field equation descriptions

Variable	Description	Transport equation
$\phi_{mp0}$	Original/initial mass of particles	$\frac{\partial}{\partial x_i}(\rho u_i \phi_{mp0}) = 0$
$\phi_M$	Moisture present in particles	$\frac{\partial}{\partial x_i}(\rho u_i \phi_M) = \frac{1}{V} \frac{dm_{evap}}{dt}$
$\phi_{VM}$	Volatile matter present in particles	$\frac{\partial}{\partial x_i}(\rho u_i \phi_{VM}) = \frac{1}{V} \frac{dm_{vol}}{dt}$
$\phi_{FC}$	Fixed carbon present in particles	$\frac{\partial}{\partial x_i}(\rho u_i \phi_{FC}) = \frac{1}{V} \frac{dm_c}{dt}$
$\phi_{ASH}$	Ash present in particles	$\frac{\partial}{\partial x_i}(\rho u_i \phi_{ASH}) = 0$
$\phi_{hp}$	Enthalpy of particle	Equation (12)

105  $\left(\frac{dm_{evap}}{dt} h_{fg}\right)$  and near surface char oxidation  $(f_{heat} \frac{dm_c}{dt} h_{rxn})$ . This gives the  
model the ability to track the particle temperature in the domain, moving the  
model away from the thermal equilibrium approach incorporated by previous  
studies using an EE approach ([22], [24] and [25]). The particle temperature  
is important in describing the sequential steps found in modelling combustion  
110 processes, especially at low boiler loads where mixing and ignition become prob-  
lematic.

## 2.2. Heat transfer modelling modelling

The radiation heat transfer is the dominant form of heat transfer found in industrial furnaces [26] and is solved by applying the gray-participating-gas and particle medium configuration of the radiation transport equation (RTE) [27] shown in equation (13).

$$\frac{dI(\vec{r}, \hat{s})}{ds} = \alpha_g \frac{\sigma_{SB} T_g^4}{\pi} - (\alpha_g + \alpha_p + \sigma_p) I(\vec{r}, \hat{s}) + \frac{\sigma_p}{4\pi} \int_{4\pi} I(\vec{r}, \hat{s}) \Phi d\Omega \quad (13)$$

In the present work the RTE is solved sing the P1 model. Ranade and Gupta [18] illustrated minimal differences between the two common radiation models (namely the P1 and discrete ordinates (DO)) for the resultant wall heat transfer rate values when modelling a 210 MWe CFPP boiler. The P1 radiation model can include the effects of particle absorption ( $\alpha_p$ ) and scattering ( $\sigma_p$ ) as well as gas mixture absorption ( $\alpha_g$ ). The P1 model transport variable is the incident

radiation ( $G - [W/m^2]$ ), and can be written for a particle laden domain as:

$$\begin{aligned} \frac{\partial}{\partial x_i} \left( \Gamma \frac{\partial G}{\partial x_i} \right) &= (\alpha_g + \alpha_p) G - 4 (\alpha_g \sigma_{SB} T_g^4 - \pi E_p) \\ \Gamma &= \frac{1}{\alpha_g + \alpha_p + \sigma_p} \end{aligned} \quad (14)$$

The flue gas absorptivity was calculated using the domain based weighted sum of gray gas model (WSGGM) using the coefficients determined by Smith et al [28]. The WSGGM accounts for the radiation emitted by tri-atomic gases, namely  $CO_2$ ,  $H_2O$  and  $SO_2$  present in the flue gas stream. The Eulerian description of the terms  $\alpha_p$ ,  $\sigma_p$  and  $E_b$  are determined using the effective number of particles ( $N_p = \rho \phi_{mp0} V / (\rho_p \pi \bar{d}_p^3 / 6)$ ) present in a cell. There formulations are given in equations (15) through (17).

$$\alpha_p = \frac{\epsilon_p A_{pn} N_p}{V} \quad (15)$$

$$\sigma_p = \frac{(1 - \epsilon_p)(1 - f_p) A_{pn} N_p}{V} \quad (16)$$

$$E_p = \frac{\epsilon_p \sigma_{SB} T_p^4 A_{pn} N_p}{V} \quad (17)$$

It is important to note that variable properties for  $(\epsilon_p)$  and  $(f_p)$  were used, that are based on the correlations of Lockwood et al [29] and Yin [30] respectively.

115

### 2.3. Process simulation model

A 1D discretized model of the furnace evaporator, platen SH, final SH, and subsequent down stream heat exchanging components was developed using Flownex SE<sup>®</sup> 2021. The model simulates the internal convection heat transfer inside the tubes and the conduction through the tube walls. The model is able to simulate the attemperation flows and momentum transport through the steam/water circuit. The heat exchangers were modelled using a two-phase mixture approach, this assumes that the fluid properties, phase velocities and temperatures are uniform per cross-sectional area. The homogeneous mixture

fraction and mixture density are defined in equations (18) and (19) respectively.

$$\alpha_H = \frac{\rho_l x}{\rho_l x + \rho_g(1 - x)} \quad (18)$$

$$\rho_M = (1 - \alpha_H)\rho_l + \alpha_H\rho_g \quad (19)$$

Applying the mixture density the following transport equations are solved;

$$\frac{\partial}{\partial t}(\rho_M A) + \frac{\partial}{\partial s}(\rho_M Au) = 0 \quad (20)$$

$$\frac{1}{A} \frac{\partial}{\partial t}(\rho_M Au) + \frac{1}{A} \frac{\partial}{\partial s}(\rho_M Au^2) = -\frac{\partial p}{\partial s} - \frac{\tau_w P}{A} - \rho_M g \frac{\partial z}{\partial s} \quad (21)$$

$$\begin{aligned} \frac{\partial}{\partial t}(\rho_M h_M) + \frac{1}{A} \frac{\partial}{\partial s}(\rho_M A u h_M) + \frac{1}{2} \frac{\partial}{\partial s}(\rho_M u^2) + \frac{1}{2A} \frac{\partial}{\partial s}(\rho_M A u^3) = \\ \frac{\partial p}{\partial t} + \frac{\dot{Q}_w}{V} - g \rho_M u \frac{\partial z}{\partial s} \end{aligned} \quad (22)$$

The process model is used to determine the required attemperation flow rates in order to achieve the exit steam conditions, the boiler efficiency, and the steam generated for each case. The results of this model aid in determining the best firing combination of burner rows for continuous low-load operation, and the effects the various cases have on the system.

### 3. Case study boiler description & set-up

In this section the numerical model configuration, for both the CFD and process model, will be explained, covering the boilers geometry, the process model set-up, the various modelling inputs (i.e. fuel characteristics and boundary conditions) and ends with the numerical solution strategy.

#### 3.1. Geometry & process model set-up

The modelled boiler is a two-pass sub-critical power boiler with a furnace depth of 13.77 [m], a width of 14.01 [m] and a height of 64 [m]. The CFD

geometric model (of Figure 1) makes use of a symmetry plane at half the width of the furnace. This was done to reduce the cell count of the numerical mesh. Both the platen and final SH are modelled as walls, with transverse pitches of 1.143 [m] and 0.8 [m] respectively. There are three levels of burners located on both the front and rear walls at heights of 11.9 [m], 19.3 [m] and 26 [m]. Figure 1 shows the modelled half of the furnace along with the locations of the platen SH, final SH, boundary walls (front, rear and side) and the domains outlet and inlets.

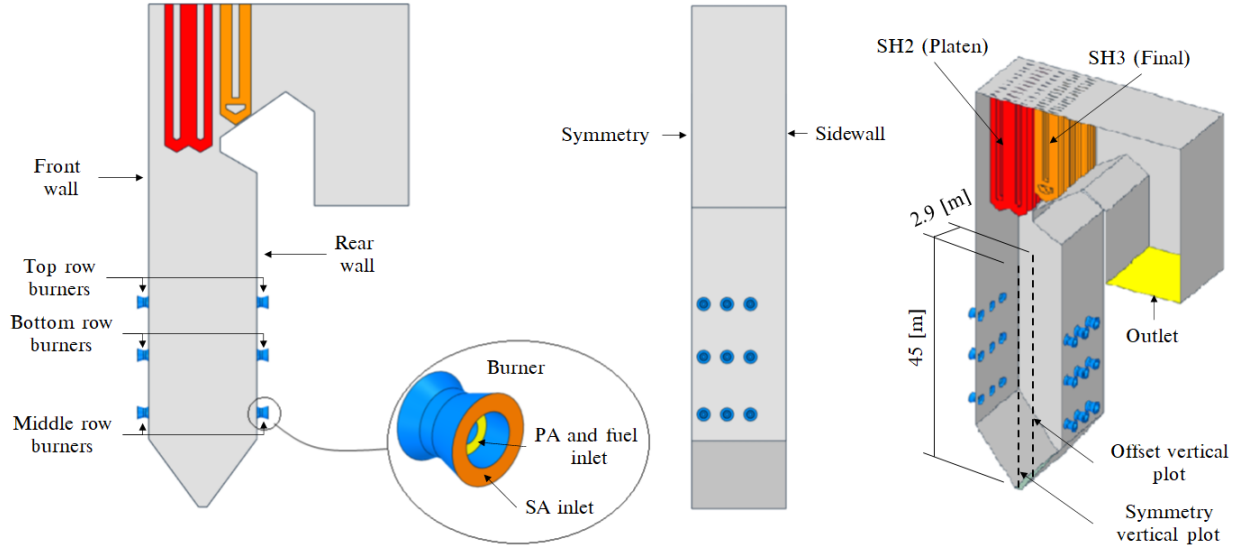


Figure 1: Boiler geometry and layout

The boiler furnace is fed by 6 mills, each supplying a pulverised fuel and primary air (PA) mixture to a burner row consisting of 6 burners. This mixture is injected through the inner burner annulus while the secondary air (SA) is fed through the outer annulus as seen Figure 1.

The process model of the boiler configuration is shown in Figure 2. The process model includes all the heat exchanging components up till and downstream of the final SH, which include the secondary reheater (RH2), primary

SH (SH1), primary reheater (RH1), economiser (EC) and the SA air heaters (SA-AH). The model includes all the relevant attenuators (ATT1, ATT2 and ATT-RH) are inlets and outlets.

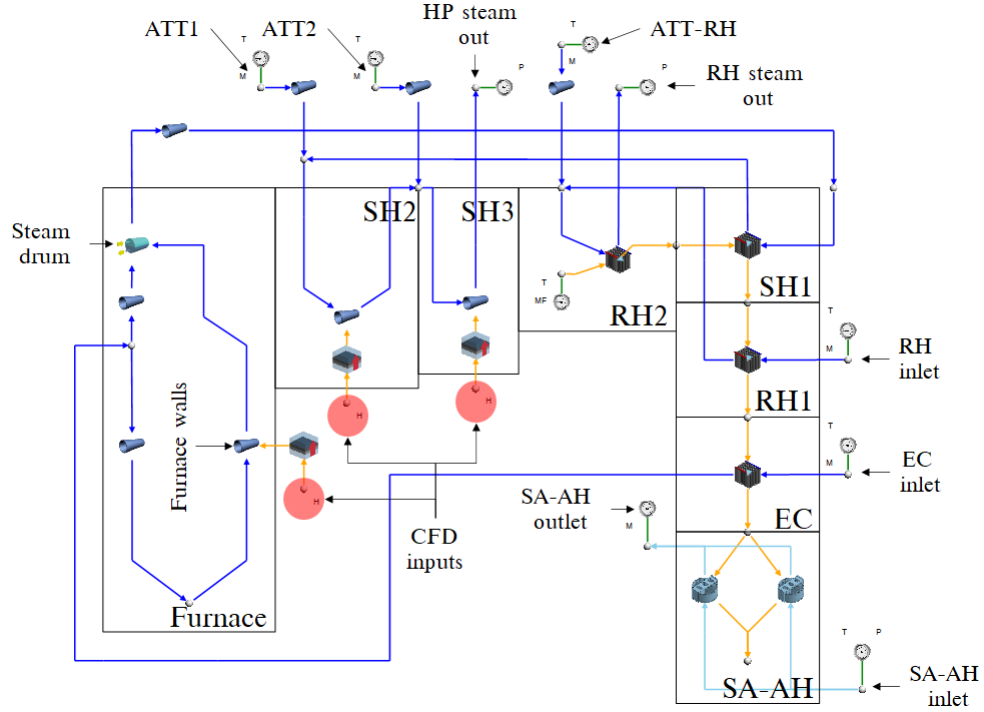


Figure 2: Process model of boiler set-up including the downstream convective components using Flownex SE 2021

150 The heat load results of the CFD simulation for the furnace, platen and final SH walls were used as inputs the process model as seen in Figure 2.

### 3.2. Model inputs

Table 2 presents the coal characteristics utilized in the current study along with the coals higher heating value (HHV).

Table 2: Utility boiler fuel characteristics

<b>Fuel constituent</b>	<b>Fraction</b>	<b>Unit</b>
<i>Ultimate analysis - (DAF)</i>	-	-
Carbon	0.7753	$kg/kg_{fuel}$
Hydrogen	0.0415	$kg/kg_{fuel}$
Nitrogen	0.0181	$kg/kg_{fuel}$
Oxygen	0.1474	$kg/kg_{fuel}$
Sulphur	0.0175	$kg/kg_{fuel}$
<i>Proximate analysis - (AR)</i>	-	-
Fixed carbon	0.340	$kg/kg_{fuel}$
Volatile matter	0.196	$kg/kg_{fuel}$
Ash	0.4090	$kg/kg_{fuel}$
Moisture	0.0550	$kg/kg_{fuel}$
<b>Energy content - (DAF)</b>	<b>Value</b>	
Higher heating value	15070	$kJ/kg_{fuel}$

155

For a 32% boiler load the current operational protocol is the to use the bottom front and rear burner rows to meet the low-load demand during start-up. For this study six cases are simulated in total with the following three burner firing configurations being utilized:

160

1. Bottom front and rear row burners are fired (Case 1 & Case 4)
2. Middle front and rear row burners are fired (Case 2 & Case 5)
3. Bottom front and middle rear row burners are fired (Case 3 & Case 6)

Two permutations of the SA flow rate, at the non-firing burners, are used for each of the firing configurations mentioned above. Table 3 shows the input

165 conditions for cases 1 to 6. The data is the result of a boilers mass and energy balance calculations.

Table 3: Case 1 to 6 model inputs on a per burner basis.

Active burners	Cases 1 - 3	Cases 4 - 6
<b>Fuel flow-rate</b> [ $kg/s$ ]	3.14	3.14
<b>PA flow-rate</b> [ $kg/s$ ]	4.95	4.95
<b>SA flow-rate</b> [ $kg/s$ ]	14.85	14.85
Non firing burners		
<b>SA flow-rate</b> [ $kg/s$ ]	5.0	2.5
Input air temperatures		
<b>PA</b> [ $K$ ]	373	373
<b>SA</b> [ $K$ ]	520	510

Table 3 shows a lower mass flow rate of SA air for case 4 to 6, this was done to compare the expected increase in boiler utilization efficiency, since less dry gas losses are expected, and the effects the drop in the flue-gas mass flow-rate has on the convective pass components modelled in the process model.

### 3.3. Numerical solution strategy

The CFD simulations were performed using ANSYS Fluent v19.5<sup>®</sup> pressure-based solver. the pressure-momentum coupling utilised the SIMPLE technique. Second-order upwinding was used to discretize the momentum, energy and species equations, whereas PRESTO! was used to discretize the pressure equation. The scalar field equations used a second-order upwind scheme.

The spatial discretization for all fields (except pressure) was set to first-order upwind for the first 1000 iterations to ensure a stable solution, after which the discretization order was increased to the above mentioned criteria. For all cases the maximum mass imbalance was 0.024 [ $kg/s$ ] for a total gas flow-rate of 190 [ $kg/s$ ] and a heat imbalance of 1770 [ $kW$ ] for a total heat input of 283 [ $MW$ ]. The remaining fields were solved till convergence.



## 4. Results & discussion

The current section will discuss the results obtained from using the above-mentioned modelling methodologies. The validity of the modelling approach will first be established by comparing the simulation results for MCR load cases (namely 100%, 80% and 60% MCR loads) to that of the experimentally obtained results of the actual plant. Once the model has been shown to demonstrate sufficient accuracy in determining the overall heat loads and combustion characteristics in the boiler furnace at varying loads, the results of the various low-load burner firing configurations are shown and discussed.

### 4.1. Model validation

The validation of the proposed model was conducted for three steady-state MCR loads of 100%, 80% and 60%. The model inputs and boundary conditions can be obtained from the study conducted by Laubscher and Rousseau [3], where using the same boiler of the present study, they evaluated the thermal performance of the heat exchanging components at full and reduced boiler loads.

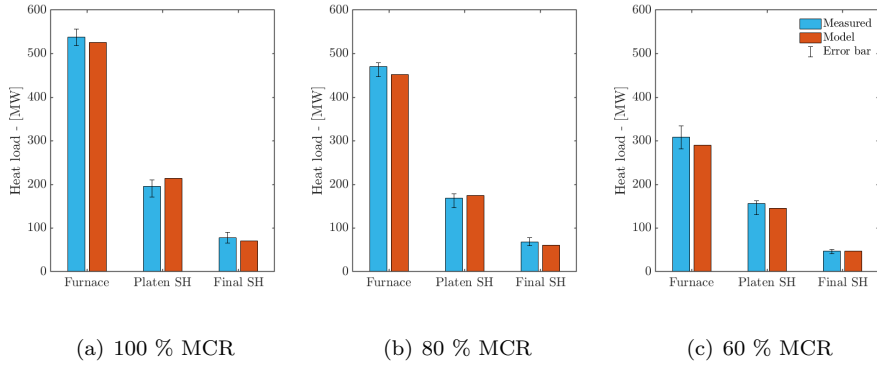


Figure 3: Comparison of experimentally calculated and model heat loads for the furnace, platen SH and final SH

In Figure 3 it is shown that the overall heat loads are in good agreement with the calculated results. For the simulated validation loads the proposed model results are within the associated error band, the general trend is an under prediction on the furnace heat loads and an over prediction on the platen super-heater. The pendant super heater illustrate the best comparable results for all load cases.

The CFD model was further validated by comparing the  $CO_{ppm}$  and  $X_{O_2}$  measurements against the CFD results. The probe measurements were taken at a furnace height of 37.5 [m] near the center of the boiler during a full load (100% MCR) operating conditions. The probe is inserted from the side walls to a depth of 4.5 [m], measurements were taken every 0.5 [m].

Figure 4 shows the averaged measurement values compared to the CFD pre-

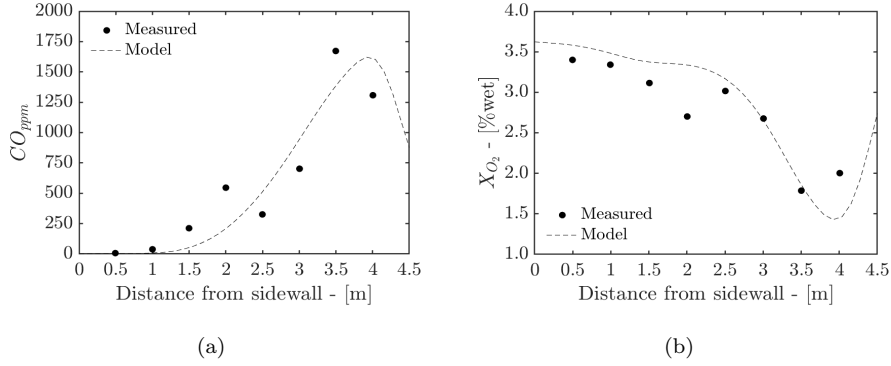


Figure 4: Experimentally calculated  $CO_{ppm}$  (a) and  $X_{O_2}$  (b) concentration predictions

dictions. It can be seen that the CFD model can sufficiently resolve the  $CO_{ppm}$  and  $X_{O_2}$  concentrations at the given probe location.

#### 4.2. Simulation results for various burner firing arrangements at 32% MCR

The temperature and velocity profiles for the various firing arrangements are shown in Figures 5 and 6 respectively. With only the middle burner rows firing (Cases 2 and 5) a substantial cold region is formed in the lower half the furnace, resulting in the lowest heat uptake. This is further exaggerated when considering Table 4 where it is illustrated that the mid-firing arrangements produce the lowest steam flow rates resulting in the lowest boiler efficiencies. The bottom firing arrangement (Cases 1 and 4) results in a high temperature zone located in the bottom half on the burner, while the mixed firing arrangement (Cases 3 and 6) results in an even distribution of high temperature gases across the furnace domain (Figure 5). This leads to the highest steam generation rate and boiler efficiency as shown in Table 4.

Table 4: Process model control parameters

	Cases					
	1	2	3	4	5	6
<b>Main steam flow-rate</b> [ $kg/s$ ]	175.8	172.9	180.5	180.2	179.1	184.1
<b>Main steam exit temp</b> [ $^{\circ}C$ ]	535	535	535	535	535	535
<b>RH steam flow rate</b> [ $kg/s$ ]	158.2	155.6	162.5	162.2	161.2	165.6
<b>RH steam exit temp</b> [ $^{\circ}C$ ]	524	527	531	512	510	520
<b>Boiler efficiency</b> [%]	85.3	84.1	87.9	87.2	85.9	89.1
<b>ATT1</b> [ $kg/s$ ]	10.4	16.9	13.9	7.9	5.5	10.9
<b>ATT2</b> [ $kg/s$ ]	1.7	3.8	4.2	3.8	3.6	4.2
<b>ATT-RH</b> [ $kg/s$ ]	0.0	0.0	0.0	0.0	0.0	0.0

Figure 7 illustrates the heat flux profiles for the simulated cases. Both cases 1 and 4 highlight high heat flux zones near the burner inlets which, in the presence of high temperatures and incomplete combustion near these regions, can lead to high-temperature corrosion [9]. An even distribution of unit heat

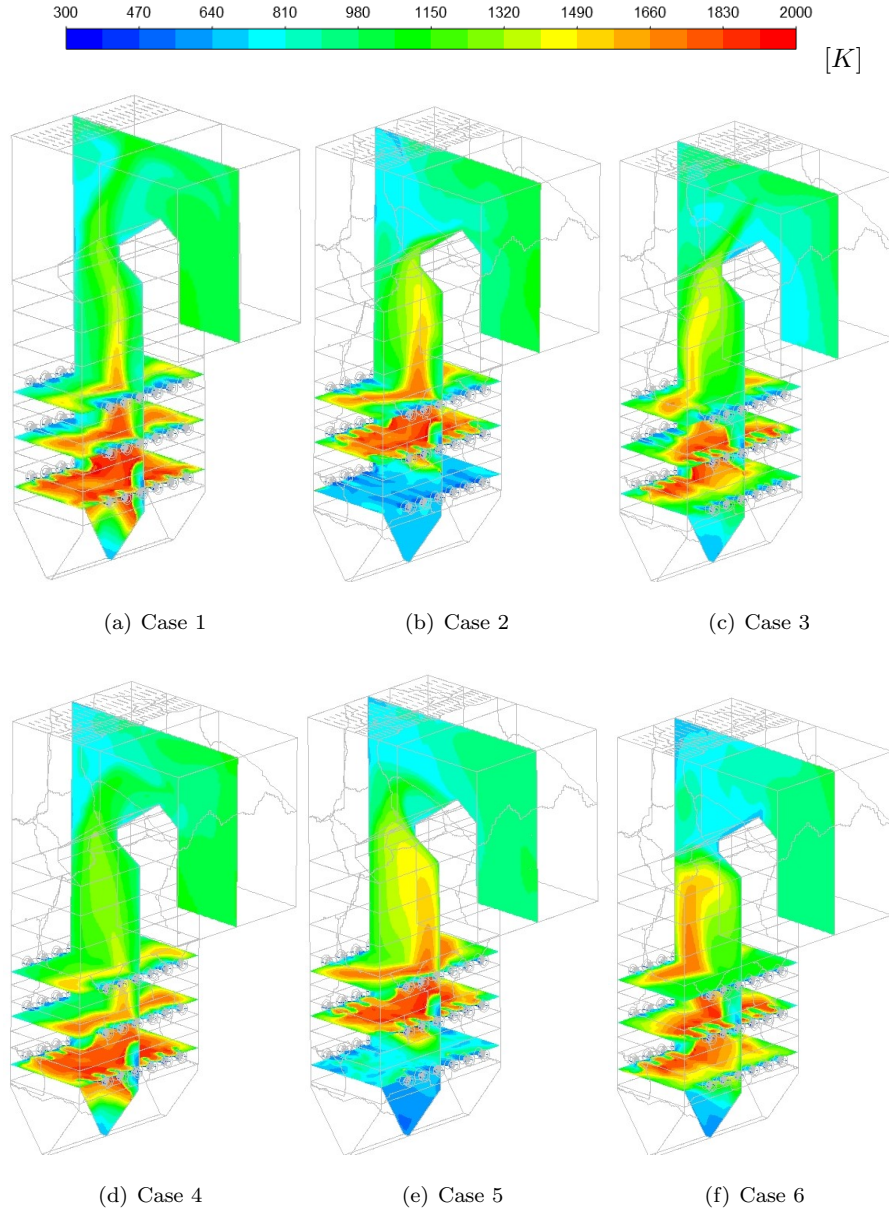


Figure 5: Temperature fields for cases 1 through 6 [(a)-(f)]

fluxes is seen in cases 3 and 6 with minimal localised heat flux concentrations being observed. Cases 2 and 5 show that most of the unit heat fluxes are absorbed in the upper half of the boiler with case 5 showing a higher heat flux

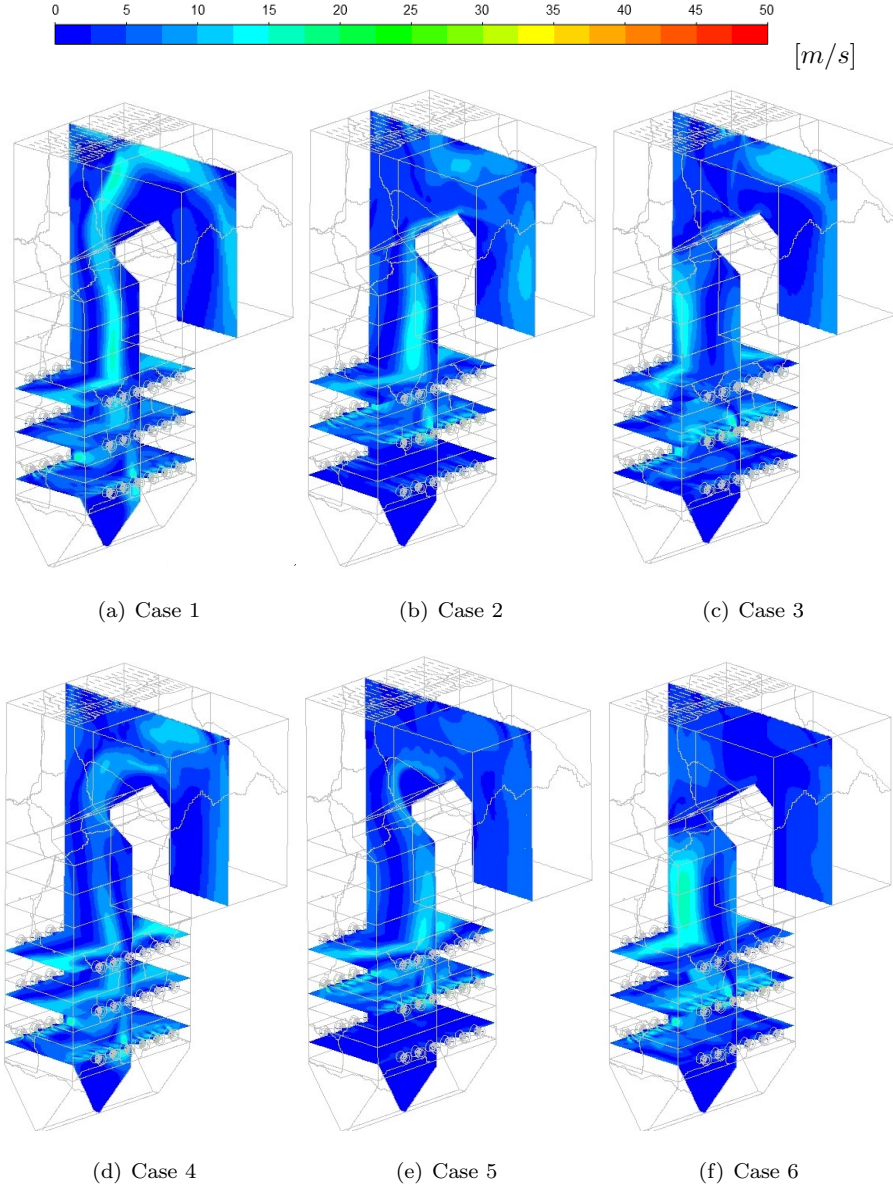


Figure 6: Velocity fields for cases 1 through 6 [(a)-(f)]

on the rear wall. This could be due the use of a lower SA flow-rate leading to velocity profiles developing closer to the rear wall, as seen in Figure 6. With this in mind a lower SA flow-rate, in general leads to hot gases and velocity

235 profiles impinging closer to the furnace walls, which can be seen in cases 4, 5 and 6 of Figures 5 and 6 respectively. With high gas temperatures and velocity impingement, cases 4, 5 and 6 (of Figure 7) experience concentrated heat fluxes around the burner inlets in comparison to corresponding cases 1, 2 and 3.

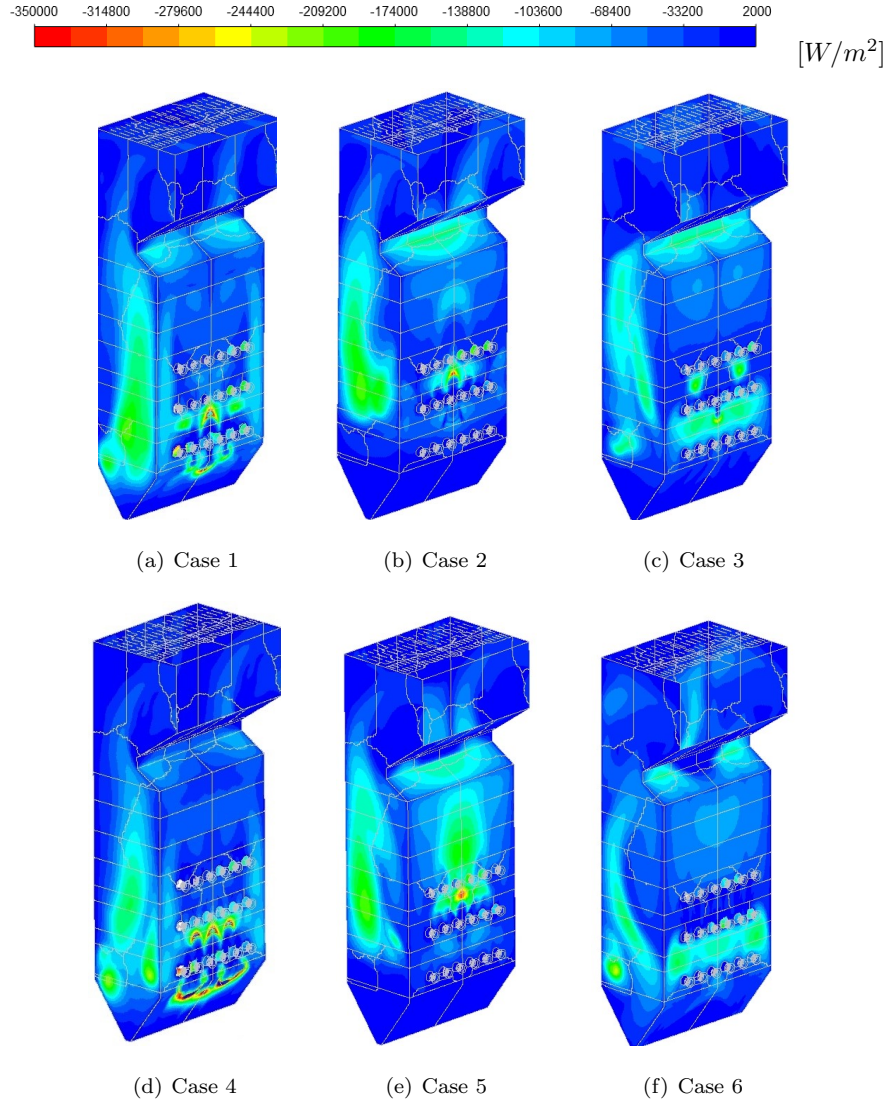


Figure 7: Heat fluxes profiles for cases 1 through 6 [(a)-(f)]

The works of Dugum et al [9], highlights the issue of high-temperature cor-

rosion caused by significant levels of  $CO$  ( $X_{CO}$  0.01 - 0.1) and no-free  $O_2$  near  
240 regions of high wall temperatures. For low-load operation this phenomena be-  
comes important to avoid since combustion instability can lead to these ideal  
circumstances. Figure 8 shows the  $CO$  molar concentration in the domain lo-  
cated on an iso-surface set 1600 [K]. The figures generally highlight the location  
and distribution of the flame core for each case. Cases 1 and 4 illustrate the high-  
245 est likelihood of high-temperature corrosion occurring near the furnace hopper,  
due to the high concentration and temperatures in that region.

Investigating the combustion stability for all the cases, the symmetry and  
offset vertical probe plots (as highlighted in Figure 1) are given in Figure 9. The  
general trends of the  $CO_{ppm}$  correspond with each cases burner firing arrange-  
250 ment, as seen with cases 3 and 6, a mixed firing arrangement, where two peaks  
are observed in the vicinity of the bottom and middle burner rows. Cases 2 and  
5 illustrates the highest  $X_{O_2}$  concentration in the lower half of the burner since  
there is minimal combustion occurring. The unburnt carbon content and exit  
flue-gas temperatures for each case are reported in Table 5. With the use of  
255 the middle burners (Cases 2 and 5) the highest exit temperature and unburnt  
carbon content is observed, since the flame core is located in the upper half of  
the furnace leading to the least possibility of complete combustion due to the  
shorter residence time. Cases 3 and 6 exhibit the best characteristics with the  
least amount of unburnt carbon content being observed. It is important to note  
260 the effects of a lower SA mass flow rate has on the furnace exit conditions for  
non-firing burners which generally leads to a hotter exit temperature as seen  
with cases 4 to 6.

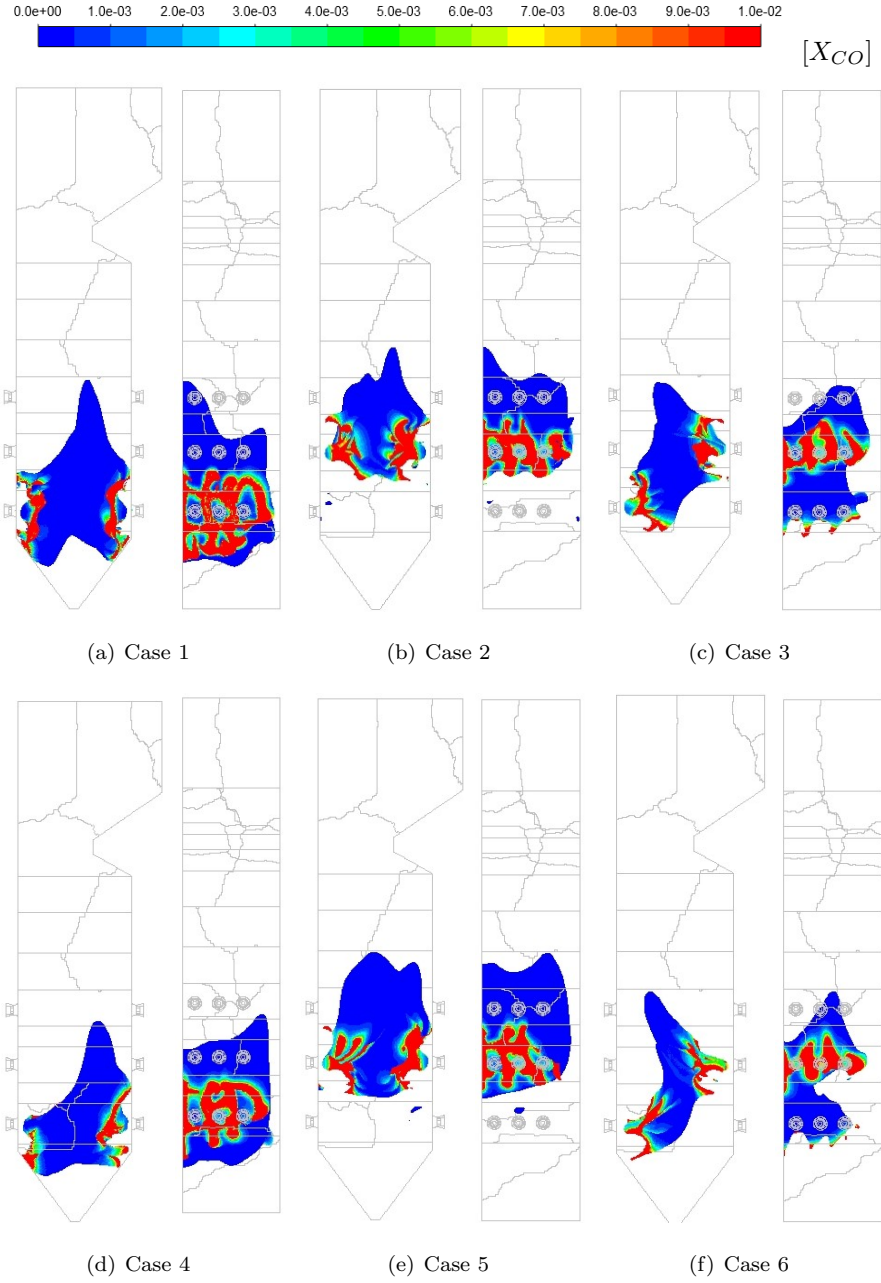
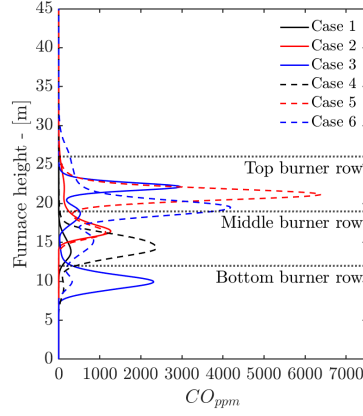
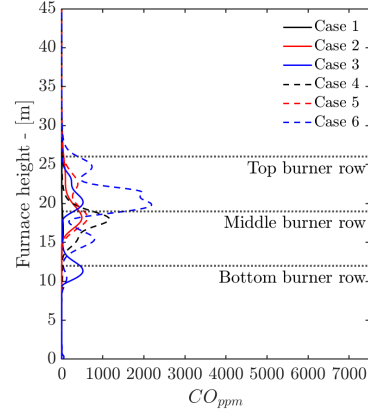


Figure 8: CO molar fraction ( $X_{CO}$ ) concentrations for cases 1 through 6 [(a)-(f)] on a temperature iso-surface of 1600 K

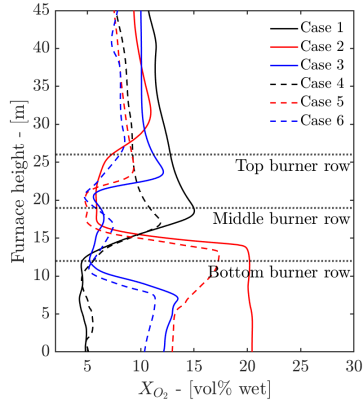




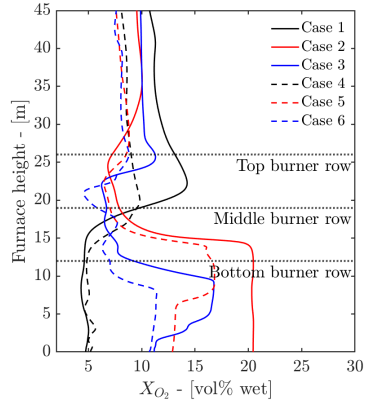
(a) Symmetry vertical plot



(b) Offset vertical plot



(c) Symmetry vertical plot



(d) Offset vertical plot

Figure 9:  $CO_{PPM}$  [(a) and (b)] and  $X_{O_2}$  [(c) and (d)] line plots on symmetry and offset vertical probe lines

Table 5: Furnace exit conditions and SH wall temperatures

	Cases					
	1	2	3	4	5	6
<i>Furnace exit</i>						
<b>Exit temperature</b> [K]	1168	1230	1215	1208	1306	1298
<b>Unburnt carbon</b> [ $(\times 10^{-3})\%$ ]	1.83	1.94	1.54	1.81	1.89	1.62
<i>Platen SH</i>						
<b>Max wall temperature</b> [ $^{\circ}C$ ]	477	492	481	480	493	490
<b>Mean wall temperature</b> [ $^{\circ}C$ ]	439	453	446	454	442	451
<i>Final SH</i>						
<b>Max wall temperature</b> [ $^{\circ}C$ ]	602	624	608	595	626	612
<b>Mean wall temperature</b> [ $^{\circ}C$ ]	520	523	517	512	520	511

The external tube metal temperatures, of Table 5, were calculated using equation 23, which takes into account the temperature drop due to the ash deposit present on platen and final SH.

$$T_{metal} = T_{wall} - \left( \frac{\dot{q}_{SH} t_{ASH}}{\lambda_{ASH}} \right) \quad (23)$$

For the platen and final SH the maximum surface temperature are observed for cases 2 and 5. For comparison a 100 % MCR load the maximum temperatures reported for the platen and final SH are of 500 [ $^{\circ}C$ ] and 623 [ $^{\circ}C$ ], with the final SH operating in the materials creep range [3]. Thus, continued operation using the firing arrangement of cases 2 and 5, could lead to SH failure.

Using the process model of Figure 2 and the results of the CFD simulations the important process control parameters were determined. Table 4 summarizes the results with the highest boiler efficiencies been observed for cases 3 and 6. With a lower SA flow-rate cases 4 to 6 exhibit a higher boiler efficiency due to the decrease in dry gas losses, when compared to cases 1 to 3. All cases exhibit adequate control of the main steam exit temperature by use of ATT1 and ATT2.

The re-heaters' exit temperature, for all cases, are determined to within the 20  
 275  $^{\circ}\text{C}$  tolerance for the intermediate turbine inlet conditions, as stipulated in the  
 design C-schedules for the plant. However, with the lack of ATT-RH control, a  
 sudden decreases in steam generation can lead to SH overheating and possible  
 SH failure. Considering all of the above, cases 3 and 6 are seen as the best firing  
 arrangements for continuous low-load operation at a load 32 % MCR.

280 Table 6 shows the radiative heat percentage of the total heat input into  
 each heat exchanger for cases 3 and 6. It can be seen that heat transfer to the  
 furnace and radiant SHs are dominated by radiation, with approximately  $\pm 10$   
 % being transferred to convection at low-load. Considering the convective pass  
 heat exchangers (RH2 through to the EC, refer to Figure 2) the convective heat  
 285 transfer becomes more apparent as seen with the reduction in radiative heat  
 transfer percentage. Case 6 tends to exhibit less convective heat transfer for  
 the said heat exchangers, due to the fact of a lower SA flow-rate for non-firing  
 burners. This will reduce the total amount of flue-gas flowing through the boiler,  
 for the same cross flow-area and similar density the velocity would be expected  
 290 to drop, reducing the convective heat transfer.

Table 6: Radiative heat transfer percentage for cases 3 and 6

	<b>Case 3</b>	<b>Case 6</b>
Furnace [%]	89.2	88.9
Platen SH (SH2) [%]	92.5	93.4
Final SH (SH3) [%]	93.5	94.0
RH2 [%]	47.6	52.2
SH1 [%]	37.2	40.7
RH1 [%]	18.7	21.5
EC [%]	5.4	6.5

## 5. Conclusions

The present study demonstrates the use of a coupled simulation used to study the effects of burner configuration at a boiler load of 32 % MCR. A validation case was performed for the developed CFD model which showed adequate results for heat fluxes to the walls, with a general tendency of the model to under-predict the heat fluxes to the furnace. The model also showed sufficient accuracy in determining the combustion characteristics at the 100 % MCR load.

The results show that using a burner arrangement that raises the position of the flame core (cases 2 and 5) increases the exit flue-gas temperature and runs the risk of final SH failure due to overheating. Subsequently, this firing arrangement also results in a higher unburnt carbon percentage at the exit flue-gas stream potentially leading to economic losses, regarding the efficient combustion of the fuel and the lowest boiler utilization efficiency.

Operation of the boiler using firing arrangements of cases 1 and 4, in relation to cases 3 and 6 results in lower boiler utilization efficiency and exit flue-gas temperature. Higher  $X_{CO}$  concentrations are observed near the bottom half of the furnace, along with high temperatures, which can lead to a high possibility of fire side corrosion occurring at continuous low-load operation using cases 1 and 4. The mixed firing arrangement, of case 3 and 6, exhibits the best boiler utilization efficiency overall. A 4.8 % decrease in unburnt carbon percentage is observed when operating using case 3 in relation to case 6. The predicted re-heater exit steam temperature of case 3 is substantially closer to the desired the temperature of 535 °C, allowing for better control.

Based on the current numerical study, carried out to determine the most favourable operating parameters and combustion stability, case 3 is seen as the optimal firing arrangement for the boiler under consideration.

## Acknowledgements

The authors would like to thank the Eskom EPPEI program for financially supporting the present study and acknowledge the computational resources pro-

320 vided by the Centre for High Performance Computing (CHPC), South Africa.

## References

- [1] A. Dugum, K. Hanjalić, Numerical simulation of coal-air mixture flow in a real double-swirl burner and implications on combustion anomalies in a utility boiler, *Energy* 170 (2019) 942–953. doi:10.1016/j.energy.2018.12.121.
- [2] Eskom Power Generation (2017).  
URL <http://www.eskom.co.za/Whatweredoing/ElectricityGeneration/Pages/Electricity{ }Generation.aspx>
- [3] R. Laubscher, P. Rousseau, CFD study of pulverized coal-fired boiler evaporator and radiant superheaters at varying loads, *Applied Thermal Engineering* 160. doi:10.1016/j.applthermaleng.2019.114057.
- [4] B. Hernik, W. Zabłocki, Numerical research of combustion with a minimum boiler load, *Archives of Thermodynamics* 41 (4) (2020) 93–114. doi:10.24425/ather.2020.135855.
- [5] J. Chang, X. Wang, Z. Zhou, H. Chen, Y. Niu, CFD modeling of hydrodynamics, combustion and NO<sub>x</sub> emission in a tangentially fired pulverized-coal boiler at low load operating conditions, *Advanced Powder Technology* 32 (2) (2021) 290–303. doi:10.1016/j.appt.2020.12.008.  
URL <https://doi.org/10.1016/j.appt.2020.12.008>
- [6] N. Modliński, K. Szczepanek, D. Nabagło, P. Madejski, Z. Modliński, Mathematical procedure for predicting tube metal temperature in the second stage reheater of the operating flexibly steam boiler, *Applied Thermal Engineering* 146 (October 2018) (2019) 854–865. doi:10.1016/j.applthermaleng.2018.10.063.
- [7] R. Laubscher, P. Rousseau, Numerical investigation into the effect of burner swirl direction on furnace and superheater heat absorption for a 620 MWe

opposing wall-fired pulverized coal boiler, *International Journal of Heat and Mass Transfer* 137 (2019) 506–522. doi:10.1016/j.ijheatmasstransfer.2019.03.150.

- 350 [8] J. Gu, Q. Liu, W. Zhong, A. Yu, Study on scale-up characteristics of oxy-fuel combustion in circulating fluidized bed boiler by 3D CFD simulation, *Advanced Powder Technology* 31 (5) (2020) 2136–2151. doi:10.1016/j.appt.2020.03.007.  
URL <https://doi.org/10.1016/j.appt.2020.03.007>
- 355 [9] Y. Du, C. Wang, Q. Lv, D. Li, H. Liu, D. Che, CFD investigation on combustion and NOx emission characteristics in a 600 MW wall-fired boiler under high temperature and strong reducing atmosphere, *Applied Thermal Engineering* 126 (x) (2017) 407–418. doi:10.1016/j.applthermaleng.2017.07.147.  
360 URL <http://dx.doi.org/10.1016/j.applthermaleng.2017.07.147>
- [10] J. Fan, L. Qian, Y. Ma, P. Sun, K. Cen, Computational modeling of pulverized coal combustion processes in tangentially fired furnaces, *Chemical Engineering Journal* 81 (1-3) (2001) 261–269. doi:10.1016/S1385-8947(00)00212-6.
- 365 [11] S. Chen, B. He, D. He, Y. Cao, G. Ding, X. Liu, Z. Duan, X. Zhang, J. Song, X. Li, Numerical investigations on different tangential arrangements of burners for a 600 MW utility boiler, *Energy* 122 (x) (2017) 287–300. doi:10.1016/j.energy.2017.01.093.
- [12] B. He, L. Zhu, J. Wang, S. Liu, B. Liu, Y. Cui, L. Wang, G. Wei, Computational fluid dynamics based retrofits to reheater panel overheating of No. 3 boiler of Dagang Power Plant, *Computers and Fluids* 36 (2) (2007) 435–444. doi:10.1016/j.compfluid.2005.09.005.  
370
- [13] Y. Jiang, B.-H. Lee, D.-H. Oh, C.-H. Jeon, Optimization of operating conditions to achieve combustion stability and reduce NOx emission at half-load

- 375 for a 550-MW tangentially fired pulverized coal boiler, *Fuel* 306 (February)  
(2021) 121727. doi:10.1016/j.fuel.2021.121727.  
URL <https://doi.org/10.1016/j.fuel.2021.121727>
- [14] S. Belošević, I. Tomanović, N. Crnomarković, A. Milićević, Full-scale CFD  
investigation of gas-particle flow, interactions and combustion in tangen-  
380 tially fired pulverized coal furnace, *Energy* 179. doi:10.1016/j.energy.  
2019.05.066.
- [15] F. Alobaid, N. Mertens, R. Starkloff, T. Lanz, C. Heinze, B. Epple, Progress  
in dynamic simulation of thermal power plants, *Progress in Energy and  
Combustion Science* 59 (2017) 79–162. doi:10.1016/j.pecs.2016.11.  
385 001.  
URL <http://dx.doi.org/10.1016/j.pecs.2016.11.001>
- [16] R. Laubscher, P. Rousseau, Numerical investigation on the impact of  
variable particle radiation properties on the heat transfer in high ash  
pulverized coal boiler through co-simulation, *Energy* 195 (2020) 117006.  
390 doi:10.1016/j.energy.2020.117006.  
URL <https://doi.org/10.1016/j.energy.2020.117006>
- [17] C. Yu, W. Xiong, H. Ma, J. Zhou, F. Si, X. Jiang, X. Fang, Numeri-  
cal investigation of combustion optimization in a tangential firing boiler  
considering steam tube overheating, *Applied Thermal Engineering* 154 (2)  
395 (2019) 87–101. doi:10.1016/j.applthermaleng.2019.03.074.  
URL <https://doi.org/10.1016/j.applthermaleng.2019.03.074>
- [18] V. Ranade, D. Gupta, Computational modeling of pulverized coal fired  
boilers, 1st Edition, Taylor & Francis, Boca Raton, 2015.
- [19] C. Sheng, B. Moghtaderi, R. Gupta, T. F. Wall, A computational fluid  
400 dynamics based study of the combustion characteristics of coal blends in  
pulverised coal-fired furnace, *Fuel* 83 (11-12) (2004) 1543–1552. doi:10.  
1016/j.fuel.2004.02.011.

- [20] M. Baum, P. Street, Predicting the combustion behaviour of coal particles, *Combustion science and Technology* 3 (43) (1971) 231.
- 405 [21] H. Knaus, U. Schnell, R. Klaus, On the modelling of coal combustion in a 550MWe coal fired utility boiler, *Progress in Computational Fluid Dynamics* 1 (2001) 194–207.
- [22] A. C. Benim, B. Epple, B. Krohmer, Modelling of pulverised coal combustion by a Eulerian-Eulerian two-phase flow formulation, *Progress in Computational Fluid Dynamics* 5 (6) (2005) 345–361. doi:10.1504/PCFD.2005.007067.
- 410 [23] H. Versteeg, W. Malalasekera, *Introduction to Computational Fluid Dynamics, The finite volume method*, 2nd Edition, Pearson Prentice Hall, 2007. doi:10.1002/9781119369189.
- 415 [24] W. Vicente, S. Ochoa, J. Aguilón, E. Barrios, An Eulerian model for the simulation of an entrained flow coal gasifier, *Applied Thermal Engineering* 23 (15) (2003) 1993–2008. doi:10.1016/S1359-4311(03)00149-2.
- [25] J. Cai, M. Handa, M. F. Modest, Eulerian-Eulerian multi-fluid methods for pulverized coal flames with nongray radiation, *Combustion and Flame* 162 (4) (2015) 1550–1565. doi:10.1016/j.combustflame.2014.11.023. URL <http://dx.doi.org/10.1016/j.combustflame.2014.11.023>
- 420 [26] P. Basu, C. Kefa, L. Jestin, *Boilers and burners: Design and theory*, 1st Edition, Springer, New York, 2000.
- [27] M. F. Modest, *Radiative Heat Transfer*, 3rd Edition, Academic Press, Kidlington, Oxford, U.K., 2013. doi:10.1016/j.neuroscience.2014.03.010.
- 425 [28] T. Smith, Z. Shen, J. Friedman, Evaluation of Coefficients for the Weighted Sum of Gray Gases Model, *Journal of Heat transfer* 104 (1982) 602–608.



- [29] F. Lockwood, S. Rizvi, N. Shah, Comparative predictive experience of coal  
430 firing, *Proceedings of the Institution of Mechanical Engineers* 200 (1986)  
79–87. doi:10.1243/PIME.
- [30] C. Yin, On gas and particle radiation in pulverized fuel combustion fur-  
naces, *Applied Energy* 157 (2015) 554–561. doi:10.1016/j.apenergy.  
2015.01.142.  
435 URL <http://dx.doi.org/10.1016/j.apenergy.2015.01.142>